PAPER

Check for updates

Aberrant photoelectric effect in the topological insulator/n-GaN heterojunction (Bi₂Te₃/n-GaN) under unpolarized illumination†

Faizan Ahmad,[a] Kavindra Kandpal, [ID][b] Roshani Singh,[c] Rachana Kumar[d] and Pramod Kumar [ID] *[c]

A topological insulator has a unique graphene-like Dirac cone conducting surface state, which is excellent for broadband absorption and photodetector applications. Experimental investigations on the Bi₂Te₃/n-GaN heterojunction exhibited an aberrant photoelectric effect under the influence of unpolarized light. Transport measurements of the Bi₂Te₃/n-GaN heterojunction revealed a negative photoconductance, with a sudden increase in resistance. This was consistent with the applied range of wavelength and power used for incident light while it was contrary to the usual gap-state transition model, which states that a negative conductance is due to the trapping of charge carriers. The observed aberrant photoelectric effect seen in Bi₂Te₃/n-GaN heterojunction devices was due to the polycrystalline nature of the Bi₂Te₃ topological insulator film, where the incident photon-induced bandgap in the Dirac cone surface state resulted in a negative photoelectric effect. This phenomenon opens the possibility for applications in highly sensitive photodetectors and non-volatile memories, along with employing the bandgap-opening concept in retinomorphic devices.

1. Introduction

Gallium nitride (GaN) as a semiconductor (SC) compound has been extensively used in electronics and optoelectronic applications.[1] It is the wide and direct bandgap SC that is mostly employed in ultraviolet (UV) detectors.[2,3] Its bandgap tunability from the infrared (0.8) to the ultraviolet (6.1 eV) makes this material fascinating for researchers.[4–6] Devices involving different quantum confinement levels are also being realized with GaN, such as single-photon emitters and other nanophotonic devices.[7,8] However, GaN-based photodetectors have limitations due to the defects and low conductivity of the material. Considering the low charge carrier mobility and the short carrier lifetime, the photosensitive area of the GaN photodiode is restricted to ∼0.1 mm², which makes it less

effective.[9–11] The search for a more effective GaN-based photodiode for overcoming these limitations is thus imperative. The major efforts at this are aimed toward creating more efficient and multifunctional devices by growing another material on GaN.[12,13] Ferromagnetic doping and the growth of other functional materials have also been realized with GaN[14] to work in this direction. Topological insulators (TIs) are a fascinating class of materials due to their exotic gapless surface states and bulk bandgap. Their surface states make them unique materials,[15] which are well protected from backscattering. Bismuth telluride (Bi₂Te₃), bismuth selenide (Bi₂Se₃), and antimony telluride (Sb₂Se₃) are some well-known three-dimensional (3D) TI materials, possessing a single Dirac cone on their surfaces.[15] High-quality Bi₂Se₃, Bi₂Te₃, and Sb₂Te₃ TI films have been fabricated by employing various methods, *e.g.* physical vapour deposition (PVD) and chemical vapour deposition (CVD) techniques on sapphire,[16] SrTiO₃,[17] Si,[18] and GaN[19] substrates. These differently grown TI film heterostructures with their unique properties find applications in spintronic devices, quantum computing, ultrafast transistors, and low-power electronic devices. Recent work in TIs is being focused on their optical study with the excellent response of their surface states to light. An enhanced performance with broadband photodetection from the infrared to the terahertz[20] has been observed in TIs due to their Dirac surface states. The

[a]Electrical, Computer and Energy Engineering, Arizona State University, Tempe, AZ-85281, USA. E-mail: faizanash1986@gmail.com
[b]Department of Electronics and Communication Engineering, IIIT-Allahabad, Prayagraj, 211012, India
[c]Spintronics and Magnetic Materials Laboratory, Department of Applied Sciences, IIIT-Allahabad, Prayagraj, 211012, India. E-mail: pkumar@iiita.ac.in
[d]ASSIST Division, CSIR-Indian Institute of Toxicology Research, Lucknow, Uttar Pradesh, 226024, India
†Electronic supplementary information (ESI) available. See DOI: https://doi.org/10.1039/d3nr03360k

warping effect-induced optical absorption and the enhanced signal-to-noise ratio (SNR) in TIs makes them analogous to graphene in photodetector applications.[21] Bi_2Te_3 is one of the interesting topological insulators[22] as a narrow bandgap (0.17 eV)[23] semiconductor, and an excellent thermoelectric material at room temperature.[24] Further, the polycrystalline Bi_2Te_3 TI film has recently been observed with multifunctional properties that are interesting for photodetection.[25] However, the Bi_2Te_3/n-GaN heterojunction has also been recognized as a good photovoltaic for mid-infrared detectors[26] and its charge carrier dynamics is favourable for optoelectronics device applications.[27] Therefore, Bi_2Te_3 and GaN seem to be appealing choices of materials for realizing heterojunctions for photodetector applications.

We grew multiple Bi_2Te_3/n-GaN heterojunctions, with a polycrystalline TI thin film on a GaN template (on sapphire). We observed an aberrant photoelectric effect in our heterojunction devices under illumination with unpolarized light. This unconventional effect, involving the negative photoconductance (NPC) phenomenon,[28,29] resulted in a reduction of the conductivity. Our results are contrary to the usual positive photoconductance (PPC) effect, where the conductivity increases with illumination. This NPC effect has been detected earlier in bulk semiconductors[28,29] and in low-dimensional structures.[30–33] However, defying all the previous explanations regarding NPC, the present aberrant effect in our heterojunction was due to the Dirac bandgap opening at the surface of the Bi_2Te_3 TI film. Further, this aberrant effect was found to be consistent for a range of optical wavelengths and powers of the incident unpolarized light. This study provides an important insight into the optical and transport study of TI-based heterojunctions for highly sensitive photodetector applications.[34,35]

2. Experimental details

An n-GaN template (thickness: 3.5 µm) on c-plane sapphire (thickness: 0.333 mm) was used as a substrate to make Bi_2Te_3/n-GaN heterojunctions. The carrier concentration in the n-GaN template was 1.9×10^{18} cm^{-3}. The substrate was prior ultrasonically cleaned with acetone, isopropanol, and de-ionized (DI) water for 10 min. A solution of $HCl : H_2O_2$ in the ratio of 1 : 2 was used to remove the constitutional oxides from the substrate followed by dipping in DI water and further drying by nitrogen gas (N_2) purging. For synthesizing the Bi_2Te_3/n-GaN heterojunction, a thin TI film of Bi_2Te_3 was grown on top of the substrate with the n-GaN film applied by a thermal coating (Scientific & Analytical Instruments) technique under a high vacuum (base pressure of 10^{-6} Torr). A powdered precursor of Bi_2Te_3 material with a purity of 99.98% (on a metal basis) was used to grow the film and to realize the Bi_2Te_3/n-GaN heterojunction. The Bi_2Te_3 film was grown on half the n-GaN film substrate by using aluminium (Al) foil masking.[36] A square molybdenum (Mo) boat was used to melt the precursor (powdered Bi_2Te_3) with the deposition parameters of

current ~60 A, time = 1 h. The crystalline phases of the TI film on the n-GaN substrate were studied using X-ray diffraction (XRD). Scanning electron microscopy (SEM) and atomic force microscopy (AFM) (Agilent Technologies, Model: 5500) were employed for studying the microstructure and morphology of the TI film grown on the GaN substrate. Raman spectroscopy was done to study the active modes of the TI film. Pump–probe spectroscopy was used to probe the transient dynamics of the charge carriers of the Bi_2Te_3 TI film grown on the n-GaN substrates. A titanium (Ti):sapphire laser amplifier with the specifications of 35 fs, 4 mJ per pulse, 1 kHz, 800 nm, was used with a 410 nm pump wavelength and the probe was varied from the visible (VB) to near-infrared (NIR) range (400–1600 nm) at 7 fs time delay with the pump. The pump power was kept low at 35 µW to make it non-destructive. The p-type of charge carriers in the Bi_2Te_3 TI film was identified using Hall measurements (8400 series, Lake Shore CRYOTRONICS) by the four-probe van der Paw method.[37] The thickness of the grown Bi_2Te_3 film was regulated by the inbuilt quartz crystal monitor in the coating unit, and confirmed by the ellipsometer (J. A. Wollam co. Inc.) to be ~150 nm. A metallic shadow mask with the cavity dimensions: diameters ~300 µm and inter distance of ~600 µm was used to make contact (thickness: 150 nm) across the Bi_2Te_3/n-GaN heterojunction. Aluminium (Al) metallic wire (purity 99.999%) was used for making the contact by thermal coating under high vacuum (10^{-6} Torr) conditions. The closest contact across the Bi_2Te_3/n-GaN heterojunction was used as two probes for the electrical characterization (Keithley 4200SCS). A tuneable light source (NewPort TLS 300XU) was used to illuminate the measurement area with different wavelengths of light. A SemiProbe probing station was used for all the electrical I–V, C–V, and C–f, and optical characterizations through two model 4225 RPM/SMU amplifiers. The detailed flow diagram describing the fabrication of the Bi_2Te_3/n-GaN heterojunction device is shown in ESI Fig. S1.† A schematic of the Bi_2Te_3/n-GaN heterostructure device is shown in Fig. 1a.

3. Results and discussion

3.1 Material and microstructural study of the Bi_2Te_3 TI film grown on n-GaN

The detailed microstructural study of the Bi_2Te_3 TI film grown on n-GaN was done by XRD and SEM. The morphology and the vibration modes were studied using AFM and Raman spectroscopy. The material study of the Bi_2Te_3 TI film is discussed with the results provided in the ESI (refer to Fig. S2 and S3 in the ESI†).

3.2 Electrical transport study

3.2.1 I–V characteristics for the Bi_2Te_3/n-GaN heterojunction. The ohmic contact is imperative in a heterojunction to examine its legitimate behaviour. A large voltage drop at the metal–semiconductor interface limits the performance of the devices.[38] For the optimum performance of the commercially
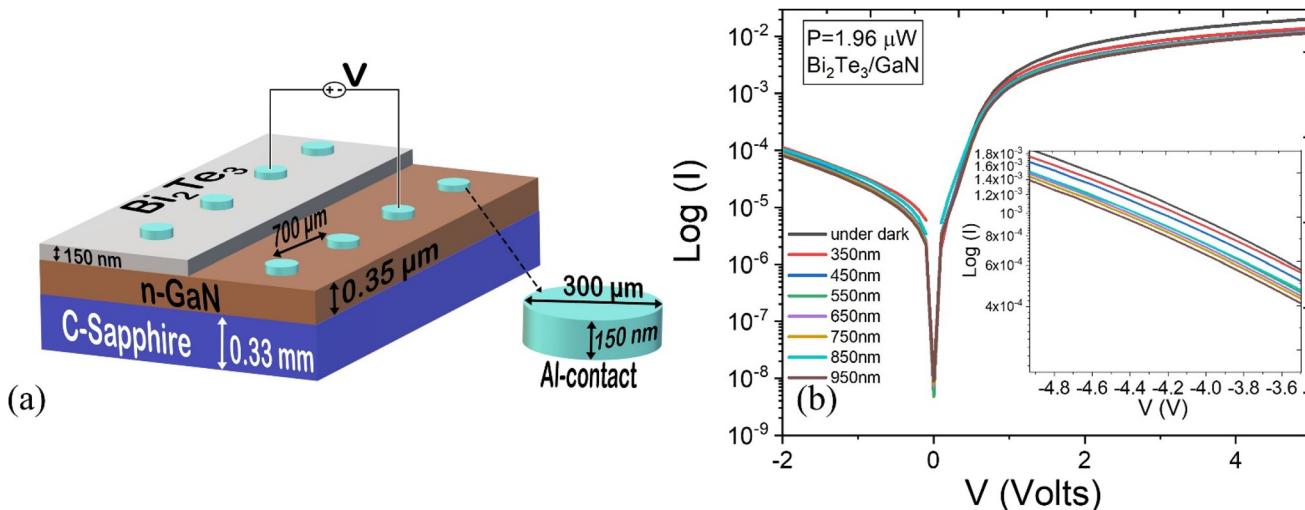
Fig. 1 (a) Schematic of the device structure of Bi_2Te_3/n-GaN/S. (b) Plot of the semi-log (I–V) characteristics for the Bi_2Te_3/n-GaN heterojunction device under dark and illumination conditions when the wavelength of the irradiating wavelength of the light was varied from 350 nm to 950 nm at a constant incident light power of 1.96 μW; inset shows the reverse saturation current in the reverse bias (V) = −4.8 V to −3.6 V.

available GaN-based devices, a large emphasis was given to the ohmic contacts. For the n-GaN template, the most suitable method for ohmic contact was to use a metal with a lower work function (W). Al with the work function W_{Al} = 4.28 eV (ref. 39) is usually preferred with n-GaN, and we thus employed it in our Bi_2Te_3/n-GaN heterojunction. The ohmic contact was validated, by the I–V results of the Al/n-GaN junction, as measured through the Al metal contacts (refer to the ESI Fig. S4b†). The Bi_2Te_3 TI film, due to its narrow band gap ($B_g \approx$ 0.17 eV),[23] formed a low resistance ohmic contact with Al.[40] The ohmic contact was also ascertained for the Al/Bi_2Te_3 junction, by I–V measurements, through the contact on the Bi_2Te_3 TI film (refer to ESI Fig. S4a†). We annealed the devices Bi_2Te_3/n-GaN after the contact deposition in the range of 200–300 °C for 1–2 h to ensure the ohmic contacts. Fig. S4a (refer to the ESI†) shows the results in both the positive and negative biases in opposite quadrants, which confirmed the ohmic behaviour and excluded the depletion layer affect. The contact was deposited symmetrically across the junction through the shadow mask to grow it identically. The measurement circuitry for the Bi_2Te_3/n-GaN heterojunction device is shown in Fig. 1a. The I–V results of the Bi_2Te_3/n-GaN heterojunction under dark conditions affirmed the rectifying nature of the device, confirming its non-ohmic nature. The I–V characteristics of the Bi_2Te_3/n-GaN heterojunction was analyzed by the standard thermionic emission (TE) theory for the device, according to which the current (I) can be expressed as:

$$I = I_R \left[\exp\left(\frac{q(V - IR_S)}{nkT}\right) - 1 \right] \quad (1)$$

where I_R is the saturation current, R_S is the series resistance, V is the operating voltage, q is the electronic charge, n is the ide-

ality factor, and k is the Boltzmann constant. The saturation current (I_R) here is given as:

$$I_R = AA^\star T^2 \exp\left(\frac{-q\varphi_b}{kT}\right) \quad (2)$$

From eqn (S2) (refer to the ESI†) and by taking the slope of the semi-log (I–V) characteristics (Fig. S5 in the ESI†) at the saturation voltage, we get the ideality factor as $n \approx 3.88$. The device area was 0.0049 cm^2, while $A^\star$ is the effective Richardson constant for n-GaN, which is 26.4 A cm^{-2} K^{-2},[41] and φ_b is the barrier height. The barrier height calculated from the by I–V method using eqn (2) was thus determined to be 0.542 eV.

3.2.2 Photoresponse of the Bi_2Te_3/n-GaN heterojunction. The Bi_2Te_3/n-GaN heterojunction behaviour was also studied under illumination. The optoelectrical study of the device was done by irradiating it with a TLS-300XU xenon light source, within the power level range of the instrument (1.5–3.78 μW). Because of the different bandgaps of n-GaN (3.4 eV)[42] and Bi_2Te_3 (0.17 eV),[23] the irradiating wavelength (λ) of the light was varied from 350 to 950 nm to observe the behavioural trend of the Bi_2Te_3/n-GaN heterojunction device. The intrusion of the thermoelectric potential was quite a possibility in our device, considering the fact that Bi_2Te_3 is an exceptional thermoelectric material with a considerable Seebeck coefficient.[43,44] Therefore, to nullify this unwanted thermoelectric potential, zero voltage was ensured between the electrodes by adjusting the spot of light without operating voltage. The I–V results of the Bi_2Te_3/n-GaN heterojunction showed an aberrant photoelectric effect with an increase in resistance in forward bias under illumination (Fig. 1b). The usual photoelectric effect in a semiconductor when stroked with an incident photon energy higher than its bandgap results in absorp-

tion of the photon, prompting the generation of electron–hole pairs with the increase in charge carrier concentration. This increase in carrier concentration increases the electrical conductivity with a reduction in the resistance of a semiconductor material. However, contrary to the established photoelectric theory, our heterojunction showed a converse behaviour under the illumination. The I–V characteristics for the Bi_2Te_3/n-GaN heterojunction showed an increase in resistance in forward biasing, under illumination with unpolarized light, compared to with the dark measurement. The reverse bias current did not change significantly but, in forward bias there was an apparent reduction in the current when the junction was illuminated. This behaviour of the heterojunction is contrary to the conventional photoelectric effect where the resistance generally decreases. This aberrant behaviour was consistent for the incident light power range (1.96–3.78 μW) and wavelength range (350–950 nm) (Fig. 1b) of the unpolarized light within the instrument limit (refer to Fig. S4 in the ESI†). This type of anomaly has been seen recently in materials having a surface Dirac cone, such as graphene[45] and TI films, due to the opening of the bandgap under illumination.[46] Theoretically, the opening of the bandgap for TIs has been illustrated under illumination with polarized light.[45,47,48] This theoretical prediction was also validated by time- and angle-resolved photoemission spectroscopy (ARPES) of the Bi_2Se_3 TI thin film surface.[49] However, we still have to go deep into the analysis of the results of the Bi_2Te_3/n-GaN heterojunction to comprehend the reason for this aberrant electrical behaviour.

The contour of the photon energy of the incident light (E) was plotted against the electric current (I) at different driving voltages in Fig. 2a. The photon energy of incident light was calculated using eqn (3) as:

$$E = \frac{hc}{\lambda} \quad (3)$$

where h is Planck's constant (6.6×10^{-34} J s^{-1}), c is the velocity of light (3.00×10^8 m s^{-1}), and λ is the wavelength of light incident on the heterojunction. Energy in quantum physics is expressed in electron volts (1 eV = 1.6×10^{-19} J). Therefore, eqn (3) can be written as E (eV) = $1.24 \times 10^3/\lambda$ (nm), where the wavelength λ is expressed in nm. The current–energy (I–E) contour plot for the Bi_2Te_3/n-GaN heterojunction power $versus$ the bias voltage (V) at 1.96 μW incident light is shown in Fig. 2a. The (I–E) contour plot showed a gradual reduction in current as we moved towards higher wavelength. As we moved towards higher energy ($E > 3.4$ eV), there was a small increase in current (Fig. 2a), which was more evident at a higher bias voltage (V). This increase in current was due to the absorption of the light energy by the n-GaN as the bandgap of n-GaN ≈3.4 eV.[42] The absorption of light energy greater than the bandgap of n-GaN of 3.4 eV resulted in an increase in charge carriers and a reduction in resistance (Fig. 2a). It was observed from the (I–E) contour plot that the aberrant photoelectric effect was apparently due to the increase in resistance and was more predominant at higher wavelength (Fig. 2a). The absorption at higher wavelength was primarily due to the absorption in the

polycrystalline TI film of Bi_2Te_3 as the bandgap of Bi_2Te_3 was approximately is 0.17 eV.[23] Therefore, from the contour plot (Fig. 2a), it could be substantially concluded that the aberrant photoelectric effect in the Bi_2Te_3/n-GaN heterojunction upon illumination (Fig. 1b) was due to the polycrystalline Bi_2Te_3 TI film. Moreover, an exclusive study on the polycrystalline Bi_2Te_3 TI film was done by studying the I–V results of the Bi_2Te_3 film using an Al ohmic contact (refer to Fig. S5 and S6 in the ESI†). The same aberrant effect was also visible with the Bi_2Te_3 TI film at higher wavelengths, which further supported our argument. This aberrant effect under illumination in the polycrystalline Bi_2Te_3 TI film (refer to Fig. S6 in the ESI†) resulted in an overall negative photoconductance (NPC) in the Bi_2Te_3/n-GaN heterojunction.

It was imperative to inquire about how this aberrant behaviour would affect the performance parameters of Bi_2Te_3/n-GaN heterojunction devices. Therefore, the responsivity (R) and detectivity (D) were calculated using eqn (4) and (5):

$$R = \frac{I_{ph}}{P_{in}} \quad (4)$$

$$D = \frac{A^{1/2}R}{\sqrt{2qI_d}} \quad (5)$$

where, I_{ph} is the photon-current (illuminated current–dark current) of the n-GaN/Bi_2Te_3 heterojunction, P_{in} is the power density of the incident light, A is the area of the device (A = 0.0049 cm^2), I_d is the electric current under dark conditions at +3 V, and q is the electrical charge. The calculated responsivity (R) from eqn (4) was plotted in contour form $versus$ the incident light energy (E) and the bias voltage (V) for the Bi_2Te_3/n-GaN heterojunction at a constant 1.96 μW incident power (Fig. 2b). Fig. 2b shows the increase in the value of responsivity (R) with the bias voltage (V). However, its value was found to be negative due to the increase in resistance under illumination. It reached towards more stability and became saturated at a higher wavelength of incident light. The higher wavelength corresponded to the polycrystalline Bi_2Te_3 TI film. The value of the responsivity for the Bi_2Te_3/n-GaN heterojunction was observed to be in the range 1.0×10^3 to 3.8×10^3 A W^{-1} for the range of bias voltage of 1–4 V. The detectivity was also calculated (eqn (5)), and is also represented by an energy-detectivity (E–D) $versus$ the driving voltage (V) contour plot (Fig. 2c) for the Bi_2Te_3/n-GaN heterojunction devices. The detectivity increased with the driving voltage and was observed to be negative due to the negative responsivity. The detectivity also stabilized towards a higher wavelength, with a slight increment at a higher driving voltage. The range of D was found to be -5.15×10^{10} to -3.86×10^{10} Jones for the operating voltage range of 1–5 V. Fig. 2d shows the responsivity and detectivity $versus$ the power density plots for the Bi_2Te_3/n-GaN heterojunction at a bias voltage (V) of 3 V and wavelength (λ) of 550 nm of incident light. It was observed that both the responsivity and detectivity exhibited an almost linear decreasing relation with the power density (P_D) of the incident light, as the power was varied from 1.96 μW to 4.20 μW. Similar negative relations for
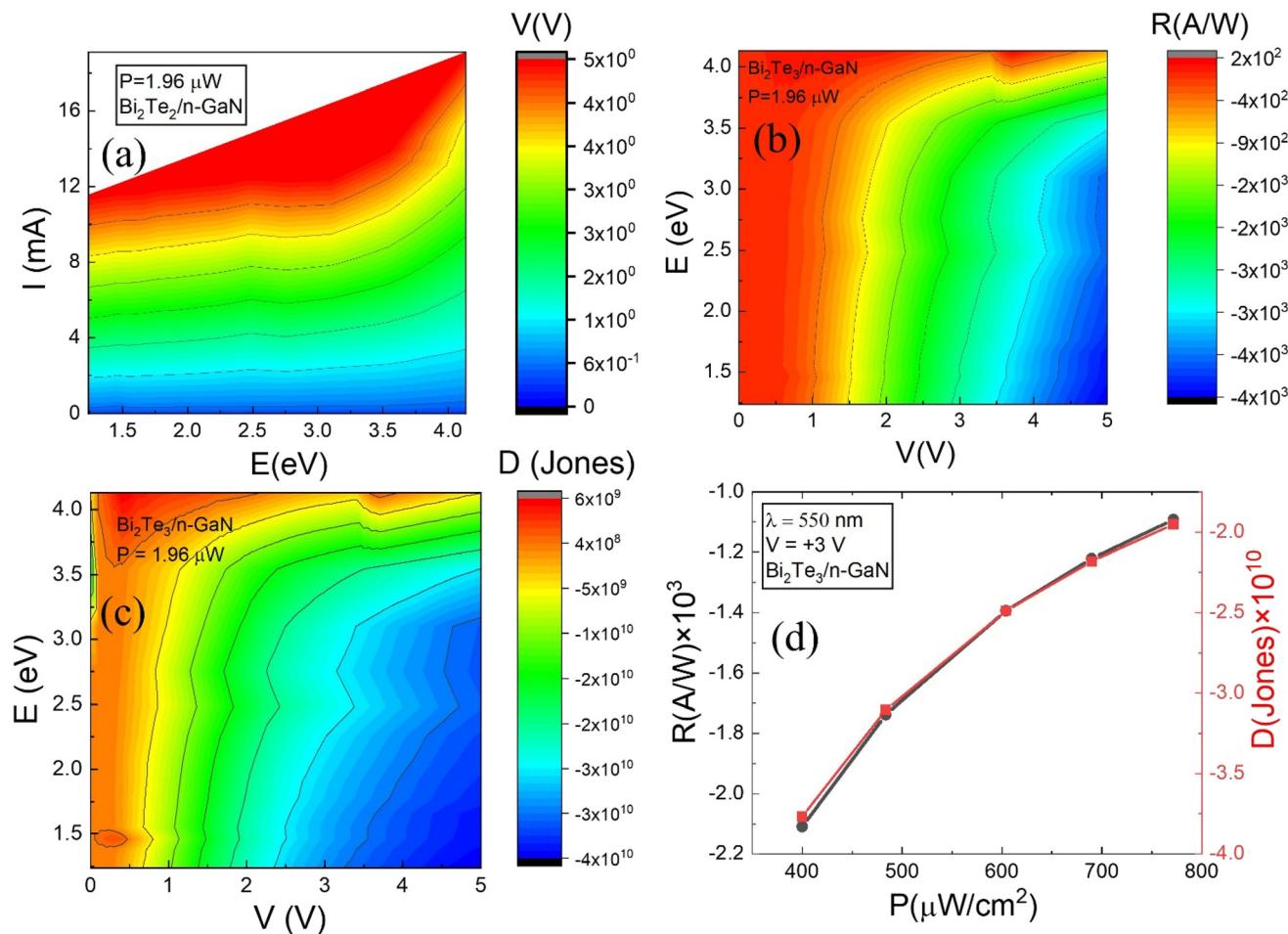
Fig. 2 (a) Contour plot showing the current–energy (I–E) plot *versus* the driving voltage (V), measured for the voltage range from V = 0–5 V for the Bi$_2$Te$_3$/n-GaN heterojunction device, where E is the incident photon energy of the light having a wavelength (λ) varied from 350 nm to 950 nm at 1.96 µW incident power. Contour plots showing the relation between the (b) energy-responsivity (E–R) *versus* the driving voltage (V) and (c) energy–detectivity (E–D) *versus* the driving voltage (V) for the Bi$_2$Te$_3$/n-GaN heterojunction device, at constant 1.96 µW incident power. (d) Plot of the responsivity–power density (R–P_D) (in black) and detectivity–power density (D–P_D) (in red) at a constant driving voltage of 3 V and wavelength of incident light (λ) of 550 nm.

R–P_D and D–P_D were also observed at other higher wavelengths (refer to Fig. S7a in the ESI†). This negative responsivity and detectivity was due to the increase in the resistance of the Bi$_2$Te$_3$/n-GaN heterojunction upon illumination, as observed in the I–V characteristics (Fig. 1b).

3.2.3 C–V, C–f, and (G_p/ω–ω) and interface study of the Bi$_2$Te$_3$/n-GaN heterojunction. The capacitance–voltage (C–V) characteristics for the Bi$_2$Te$_3$/n-GaN heterojunction are shown in Fig. 3a. No hysteresis behaviour was detected when the voltage was swept from −5 V to +5 V and then from +5 V to −5 V. The C–V characteristics appeared to be shifted towards more positive bias from the origin, which may be due to the presence of interface states.[50] The capacitance dependence on the biasing (V) became less pronounced at high voltage biasing (V > 2 V). The capacitance (C) was observed to be higher at lesser frequency due to the interface states following the alternating current (AC) signal. The carrier concentration and barrier height of the Bi$_2$Te$_3$/n-GaN heterojunction was determined

from the slope and the intercept of the $1/C^2$–V plot, as shown in Fig. 3b, and as determined by using the following equations:

$$\frac{1}{C^2} = \frac{2}{q e \varepsilon A^2 N_D}(V_{bi} - V) \qquad (6)$$

where the electric permittivity ε = 0.65ε_0 [51] for the Bi$_2$Te$_3$ TI film, the permittivity of free space (ε_0) = 8.85 × 10^{-12} F m^{-1}, V_{bi} is the built-in potential, and N_D is the carrier concentration in the film, while the barrier height (φ_b) of the heterojunction given by eqn (7) as:

$$\varphi_b = V_{bi} + \frac{kT}{q}\left(\frac{N_C}{N_D}\right) \qquad (7)$$

where $N_c = 2\left(\frac{2\pi m^* kT}{h^2}\right)^{3/2} = 2.24 \times 10^{18}$ cm^{-3} is the conduction band density of states at T = 300 K. Using eqn (6) and (7),
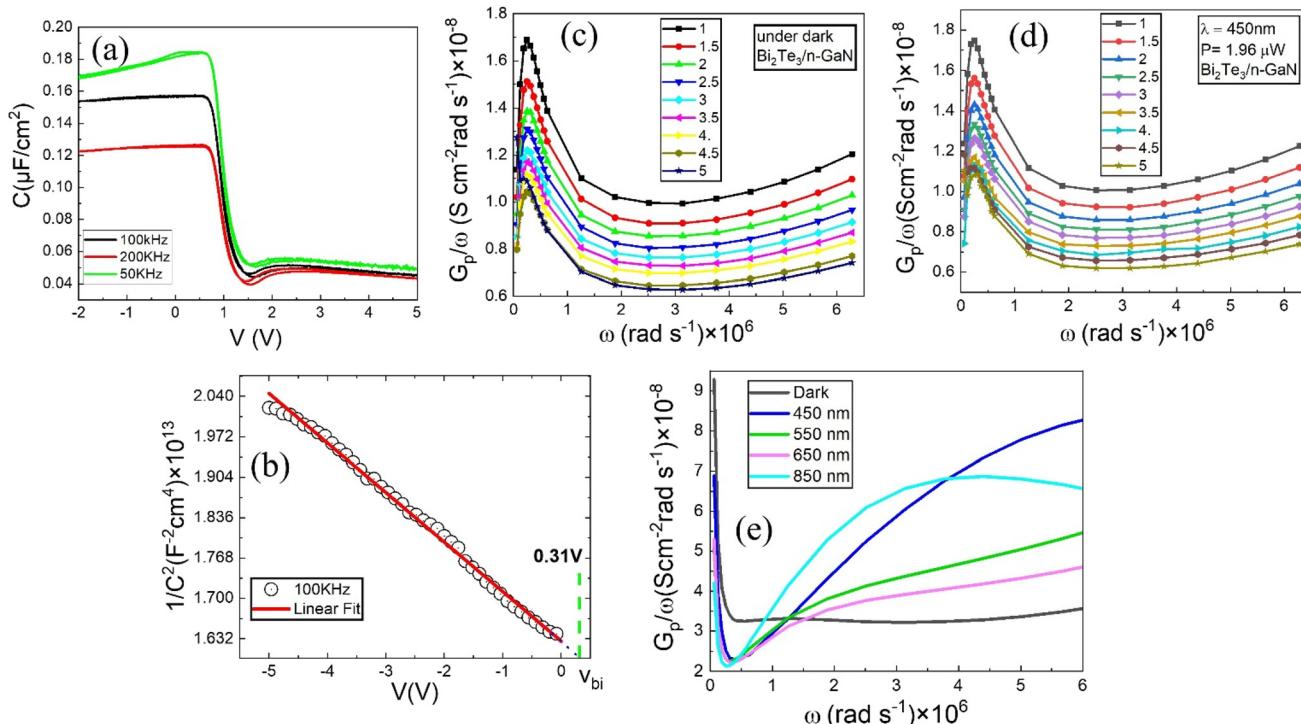
**Fig. 3** (a) Capacitance–voltage (C–V) characteristics for the Bi_2Te_3/n-GaN heterojunction under dark conditions at constant frequencies of 50, 100, and 200 kHz with the driving voltage from −2 V to +5 V. (b) Plot of $1/C^2$–V for the Bi_2Te_3/n-GaN heterojunction at 100 kHz frequency, with the intercept on the x-axis showing the built-in voltage (V_{bi}). (c) Plot of the conductance/radial frequency (G_p/ω) *versus* radial frequency (ω) for the Bi_2Te_3/n-GaN heterojunction, measured for the voltage biasing from +1 V to +5 V (interval of 0.5 V) under the dark conditions and (d) under light (λ = 450 nm, power = 1.96 W). (e) Conductance/radial frequency (G_p/ω) *versus* radial frequency (ω) plot for the Bi_2Te_3/n-GaN heterojunction at a constant positive bias of 0.5 V under the dark and illuminated conditions (∼450−850 nm, P = 1.96 μW).

the carrier concentration (N_D) and the barrier height (φ_b) were calculated and found to be 3.89×10^{16} cm^{-3} and 1.80 eV. The barrier height obtained by the C–V measurement was comparatively higher than that measured by the I–V measurement. This discrepancy was primarily due to the surficial or interface defects, as observed in the C–V characteristics by the positive shift (Fig. 3a). This variation in barrier height might also be possible due to the image force and the barrier inhomogeneities as seen earlier.[52]

The $1/C^2$–V plot for the Bi_2Te_3/n-GaN heterojunction (Fig. 3b) showed a linear relation in the reverse bias of the Bi_2Te_3/n-GaN heterojunction. The good linear fitting in the reverse bias indicated the near absence of surface states, which affected the linearity of the $1/C^2$–V plot in the case of the charging and discharging of the traps.[53] The capacitance–frequency (C–f) plot (refer to Fig. S7b in the ESI†) showed an almost linear decrease in the capacitance under reverse bias, without any major peak, confirming the negligible presence of traps in this region.[53] To further study the trap characteristics, including the trap levels and the trap density, frequency (f) dependence conductance (G_p) measurements were performed. Here, G_p/ω *versus* the radial frequency ($\omega = 2\pi f$) was plotted to study the trap density and trap response time.[53] The G_p/ω–ω plot for the Bi_2Te_3/n-GaN heterojunction under the dark and under illuminated conditions in reverse bias was studied (refer

to Fig. S7c and S7d in the ESI†), and it was observed that G_p/ω monotonically decreased without any peaks, with the least dependence on the negative biasing at a higher frequency. A similar behaviour for the heterojunction was observed by the G_p/ω–ω plot, under both dark and illuminated conditions (refer to Fig. S7c and d in the ESI†). The negative biasing reinforces the negligible charge and discharge of the trapping process. The G_p/ω–ω plot for the Bi_2Te_3/n-GaN heterojunction in positive bias is shown in Fig. 3c and d for the voltage range +1 V to +5 V (interval of 0.5 V), under both dark and illuminated conditions (λ = 450 nm, P = 1.96 μW). A single G_p/ω sharp peak at the same frequency ($\omega = 2.5 \times 10^6$ rad s^{-1}) was observed within the measured voltage bias. The peaks implied the presence of a trap state with a single discrete energy. The G_p/ω peaks here decreased with the increase in the applied positive bias. Here, the peaks in G_p/ω represented the trap density, which reduced with increasing the applied positive bias. The illuminated Bi_2Te_3/n-GaN heterojunction (λ = 450 nm, P = 1.96 μW) showed almost the same G_p/ω–ω characteristics without any shifting of the G_p/ω peaks. This similar peak pattern was also observed for all the measured ranges of incident light wavelength (λ) from 450–950 nm. A shift in the G_p/ω peaks was not observed, which was expected after the illumination due to the rise in temperature as observed in the previous study.[53] The G_p/ω–ω characteristics for the Bi_2Te_3/

n-GaN heterojunction at +0.5 V bias voltage are shown in Fig. 3e, under dark and illuminated conditions (λ = 450–850 nm, P = 1.96 μW). Interestingly, only a single G_p/ω minimum was observed at the frequency $\omega = 0.5 \times 10^6$ rad s^{-1} when the wavelength was varied over the range from 450–850 nm, signifying the minimum density of traps. The illuminated G_p/ω minima peak, however, dipped more in comparison to the dark one, due to the decrease in the conductivity under illumination (Fig. 3e). This dip in the peak was consistent with a reduction in current seen in the $I–V$ results of the Bi$_2$Te$_3$/n-GaN heterojunction (Fig. 1b). This reduction in current could also be observed from the ($I–E$) versus V contour plot at higher incident photon wavelength (Fig. 1b) due to the polycrystalline Bi$_2$Te$_3$ TI film in the Bi$_2$Te$_3$/n-GaN heterojunction.

3.2.4 Energy band of Bi$_2$Te$_3$/n-GaN heterojunction under dark and illuminated conditions. Fig. 4 shows the energy band diagram for the Bi$_2$Te$_3$/n-GaN heterojunction under the

Fig. 4 Energy band diagram of the Bi$_2$Te$_3$/n-GaN heterojunction at (a) thermal equilibrium, where a space charge region was created due to the diffusion of carriers at the junction resulting in built-in potential at the junction, (b) forward biasing under the dark conditions with the Dirac cone surface state of the polycrystalline Bi$_2$Te$_3$ TI film, and (c) forward bias under the influence of the light photons, where the shape of the Dirac cone changed with the opening of bandgap at the surface of the polycrystalline Bi$_2$Te$_3$ TI film under illumination.

thermal equilibrium and at forward biasing under dark and illumination conditions. Here, E_c, E_V, E_f are the notations used for the conduction band, valence band, and Fermi energy level of the respective material, and E_g ~0.17 eV (ref. 23) and E_g ~3.4 eV (ref. 42) was the bandgap of the Bi$_2$Te$_3$ and n-GaN. Fig. 4a shows the band alignment of the Bi$_2$Te$_3$/n-GaN heterojunction under thermal equilibrium with the creation of a space charge region resulting in the built-in potential. Under forward biasing, the n-GaN bands were shifted upwards compared to the Bi$_2$Te$_3$ with the increase in the forward current. The Dirac cone surface showed the surface state of the polycrystalline Bi$_2$Te$_3$ TI film (Fig. 4b) dominated the overall transport due to the large bulk resistance, thereby masking the bulk properties. The increase in resistance in the $I–V$ results could be mainly attributed to the increase in the resistance in the polycrystalline Bi$_2$Te$_3$ TI films under light illumination, due to absorption of the light of higher wavelength (refer to Fig. S6b in the ESI†). This increase in resistance in the polycrystalline Bi$_2$Te$_3$ TI films could be attributed to the opening of the bandgap in the Dirac cone surface, as shown in Fig. 4c. Such bandgap opening has also been seen recently for incident unpolarized light, resulting in an anomalous photoelectric effect in a polycrystalline Bi$_2$Te$_3$ TI film.[46] Furthermore, this opening of the bandgap in the Dirac cone surface of the Bi$_2$Te$_3$ TI film was due to the electron and holes recombination with spin up and spin down, generating an energy gap in the Dirac cone surface (Fig. 4c). This structure and the recombination could possibly be explained on the basis of the two Dirac cone surface states[54] (refer to Fig. S11 in the ESI†) derived from the ultrafast spectroscopic results of the Bi$_2$Te$_3$/n-GaN heterojunction. It was shown how the spin polarized electrons get injected into the Bi$_2$Te$_3$ film and the overall dominance was that of the surface current due to the suppression of the bottom surface current (refer to section 6 in the ESI†).

Conceptually, the opening of the bandgap of the Dirac cone was substantiated for graphene and TIs under the illumination with polarized light.[45,47,48,55] These band openings under circularly polarized light have also been observed through experimental time and angle-resolved photoemission spectroscopy (ARPES) of Bi$_2$Se$_3$ TI thin films.[49] However, contrary to the observation under polarized light, the phenomenon observed here was due to the unpolarized light, which makes it more interesting. The polycrystalline Bi$_2$Te$_3$ film has the same rhombohedral crystal structure as the single crystal in the space group D_{3d}^5 ($R\bar{3}m$)[56] with the time-reversal symmetry. Therefore, our polycrystalline had a similar Dirac cone-like structure as the single-crystal Bi$_2$Te$_3$ and behaved similarly under the influence of light with the opening of the bandgap. Due to the intrinsic defects present in the undoped Bi$_2$Te$_3$ films, their Fermi level lay in the conduction band of the bulk, giving the material a metallic nature, and therefore the thermal effect caused by the illumination could not be completely ignored. This thermal effect enhanced the resistance through electron–phonon scattering.[46] Nevertheless, the instant positive resistance effect could not be seen in the $G_p/\omega–\omega$ characteristics (Fig. 3c & d), where the peak shifting was not apparent. The

thermal artefact was also not seen recently in a photodetection study of polycrystalline Bi_2Te_3 TI films due to the lack of a long tail in the transient response.[46] Furthermore, a weak broadening of the topological surface state with the temperature and negligible anomalies in the dispersion of the state were observed for the Bi_2Te_3 TI recently.[57] Therefore, this remarkably weak electron–phonon coupling in the Bi_2Te_3 films further excluded the thermal origin of the increase in the resistance in our experiment.

The previously proposed model to describe the negative photoconductivity (NPC) effect[28,58] explained the trapping of electrons by a vacant localized state of random fluctuations in the local potential barrier.[46] According to this gap-state transition model, the negative photoconduction should be observed because of the trapping of the photoexcited electrons,[33,34] with the occurrence of negative photoconduction at a particular photon energy. However, it was observed that the intrinsic negative photoconductivity response for our Bi_2Te_3 TI heterojunction devices prevailed over a broad range of incident light wavelengths and power. Therefore, based on our experimental evidence, we emphasize that the observed aberrant photoelectric effect in our Bi_2Te_3/n-GaN heterojunction devices was due to the intrinsic feature of the polycrystalline Bi_2Te_3 TI film under illumination. This new mechanism involved in our results was certainly due to the opening of the bandgap at the Dirac cone surface of the polycrystalline Bi_2Te_3 TI film under the influence of unpolarized light; thereby decreasing the surface charge mobility and increasing the resistance as compared to the dark current, and therefore resulting in an aberrant photoconduction in our Bi_2Te_3/n-GaN heterojunction devices. We observed a considerable negative photoresponse and high responsivity for our Bi_2Te_3/n-GaN heterojunction device. NPC devices have been lately employed for the fabrication of humidity and light sensors.[59] Due to its high responsivity, our Bi_2Te_3/n-GaN device can likely find applications in highly sensitive photodetectors[60] and non-volatile memories.[61–63] Also, perhaps the bandgap-opening phenomenon in the presence of the unpolarized light can be employed in retinomorphic devices.[64]

4. Conclusion

The Bi_2Te_3/n-GaN heterojunction was realized by growing a thin polycrystalline Bi_2Te_3 TI film on an n-GaN template (on sapphire). The I–V characteristics confirmed the rectifying nature of the heterojunction device. The electrical properties of the heterojunction were studied by I–V, C–V, C–f, and G_p/ω–ω plots under both the dark and illuminated conditions. The optical study of the Bi_2Te_3/n-GaN heterojunction devices revealed an aberrant photoelectric effect under a broad range of incident light wavelengths and power. The negative photoconductance was observed in the I–V characteristics with an increase in resistance under the influence of unpolarized light in the forward bias. The good responsivity and detectivity of -3.8×10^3 A W^{-1} and -3.86×10^{10} Jones were observed in the

working range of the device. The observed aberrant photoelectric effect under unpolarized illumination was due to a photon-induced gap at the Dirac point on the polycrystalline Bi_2Te_3 TI film surface, resulting in negative photoconductivity. The observed aberrant photoelectric effect can be significant in realizing highly sensitive photodetectors and non-volatile memories; while the band gap opening can be employed in applications in retinomorphic devices with atypical ranges of operation.

Author contributions

P. K. and F. A. conceived the initial research idea planned the study. P. K. and F. A. did the electrical analysis. F. A., K. K., P. K. wrote the manuscript. R. K. analyzed the ultrafast data.

Conflicts of interest

No conflict of interest from any of the authors.

Acknowledgements

References

1 B. Zhang and Y. Liu, *Chin. Sci. Bull.*, 2014, **59**, 1251–1275.

2 B.-J. Kim, G. Yang, H.-Y. Kim, K. H. Baik, M. A. Mastro, J. K. Hite, C. R. Eddy, F. Ren, S. J. Pearton and J. Kim, *Opt. Express*, 2013, **21**, 29025–29030.

3 M. Kumar, H. Jeong, K. Polat, A. K. Okyay and D. Lee, *J. Phys. D: Appl. Phys.*, 2016, **49**, 275105.

4 Y.-C. Yao, C.-Y. Huang, T.-Y. Lin, L.-L. Cheng, C.-Y. Liu, M.-T. Wang, J.-M. Hwang and Y.-J. Lee, *Microelectron. Eng.*, 2015, **138**, 1–6.

5 Y. Jiang, Y. Li, Y. Li, Z. Deng, T. Lu, Z. Ma, P. Zuo, L. Dai, L. Wang and H. Jia, *Sci. Rep.*, 2015, **5**, 1–7.

6 H. J. Chang, T. W. Chen, J. W. Chen, W. C. Hong, W. C. Tsai, Y. F. Chen and G. Y. Guo, *Phys. Rev. Lett.*, 2007, **98**, 136403.

7 L. Zhang, T. A. Hill, C.-H. Teng, B. Demory, P.-C. Ku and H. Deng, *Phys. Rev. B: Condens. Matter Mater. Phys.*, 2014, **90**, 245311.

8 A. K. Viswanath, *J. Nanosci. Nanotechnol.*, 2014, **14**, 1253–1281.

9 C.-J. Lee, S.-B. Kang, H.-G. Cha, C.-H. Won, S.-K. Hong, B.-J. Cho, H. Park, J.-H. Lee and S.-H. Hahm, *Jpn. J. Appl. Phys.*, 2015, **54**, 06FF08.

10 F. Lin, S.-W. Chen, J. Meng, G. Tse, X.-W. Fu, F.-J. Xu, B. Shen, Z.-M. Liao and D.-P. Yu, *Appl. Phys. Lett.*, 2014, **105**, 73103.

11 A. Gundimeda, S. Krishna, N. Aggarwal, A. Sharma, N. D. Sharma, K. K. Maurya, S. Husale and G. Gupta, *Appl. Phys. Lett.*, 2017, **110**, 103507.

12 M. Rais-Zadeh, V. J. Gokhale, A. Ansari, M. Faucher, D. Théron, Y. Cordier and L. Buchaillot, *J. Microelectromech. Syst.*, 2014, **23**, 1252–1271.

13 M. Wu, Z. Gong, A. J. C. Kuehne, A. L. Kanibolotsky, Y. J. Chen, I. F. Perepichka, A. R. Mackintosh, E. Gu, P. J. Skabara and R. A. Pethrick, *Opt. Express*, 2009, **17**, 16436–16443.

14 S. Dhar, O. Brandt, M. Ramsteiner, V. F. Sapega and K. H. Ploog, *Phys. Rev. B*, 2005, **72**, 245203.

15 Y. L. Chen, J. G. Analytis, J. H. Chu, Z. K. Liu, S. K. Mo, X. L. Qi, H. J. Zhang, D. H. Lu, X. Dai and Z. Fang, *Science*, 2009, **325**, 178–181.

16 K. Zheng, L.-B. Luo, T.-F. Zhang, Y.-H. Liu, Y.-Q. Yu, R. Lu, H.-L. Qiu, Z.-J. Li and J. C. A. Huang, *J. Mater. Chem. C*, 2015, **3**, 9154–9160.

17 P. H. Le, K. H. Wu, C. W. Luo and J. Leu, *Thin Solid Films*, 2013, **534**, 659–665.

18 Y. Li, G. Wang, X. Zhu, M. Liu, C. Ye, X. Chen, Y. Wang, K. He, L. Wang and X. Ma, *Adv. Mater.*, 2010, **22**, 4002–4007.

19 D. Minjiang, G. Hu, L. Li and Y. Zhang, *Nano Energy*, 2018, **50**, 544–551.

20 X. Zhang, J. Wang and S.-C. Zhang, *Phys. Rev. B: Condens. Matter Mater. Phys.*, 2010, **82**, 245107.

21 J. M. Shao, H. Li and G. W. Yang, *Nanoscale*, 2014, **6**, 3513–3517.

22 J. Ma, K. Deng, L. Zheng, S. Wu, Z. Liu, S. Zhou and D. Sun, *2D Mater.*, 2019, **6**, 32001.

23 E. Kioupakis, M. L. Tiago and S. G. Louie, *Phys. Rev. B: Condens. Matter Mater. Phys.*, 2010, **82**, 245203.

24 I. T. Witting, T. C. Chasapis, F. Ricci, M. Peters, N. A. Heinz, G. Hautier and G. J. Snyder, *Adv. Electron. Mater.*, 2019, **5**, 1800904.

25 J. D. Yao, J. M. Shao, S. W. Li, D. H. Bao and G. W. Yang, *Sci. Rep.*, 2015, **5**, 1–8.

26 M. Y. Pang, W. S. Li, K. H. Wong and C. Surya, *J. Non-Cryst. Solids*, 2008, **354**, 4238–4241.

27 R. P. Prasankumar and A. J. Taylor, *Optical techniques for solid-state materials characterization*, CRC Press, 2016.

28 P.-C. Wei, S. Chattopadhyay, M.-D. Yang, S.-C. Tong, J.-L. Shen, C.-Y. Lu, H.-C. Shih, L.-C. Chen and K.-H. Chen, *Phys. Rev. B: Condens. Matter Mater. Phys.*, 2010, **81**, 45306.

29 M. Liao, Y. Koide, J. Alvarez, M. Imura and J.-P. Kleider, *Phys. Rev. B: Condens. Matter Mater. Phys.*, 2008, **78**, 45112.

30 A. S. Chaves and H. Chacham, *Appl. Phys. Lett.*, 1995, **66**, 727–729.

31 H. Nakanishi, K. J. M. Bishop, B. Kowalczyk and A. Nitzan, *Nature*, 2009, **460**, 371–375.

32 X. Zhang, J. Jie, Z. Wang, C. Wu, L. Wang, Q. Peng, Y. Yu, P. Jiang and C. Xie, *J. Mater. Chem.*, 2011, **21**, 6736–6741.

33 E. Baek, T. Rim, J. Schütt, C. Baek, K. Kim, L. Baraban and G. Cuniberti, *Nano Lett.*, 2017, **17**, 6727–6734.

34 Y. Yang, X. Peng, H.-S. Kim, T. Kim, S. Jeon, H. K. Kang, W. Choi, J. Song, Y.-J. Doh and D. Yu, *Nano Lett.*, 2015, **15**, 5875–5882.

35 G. Kim, I. G. Kim, J. H. Baek and O. K. Kwon, *Appl. Phys. Lett.*, 2003, **83**, 1249–1251.

36 F. Ahmad, K. Kandpal, N. Kumar, R. Kumar and P. Kumar, *IEEE Trans. Electron Devices*, 2020, **67**(12), 5388–5395.

37 F. Ahmad, S. Singh, S. K. Pundir, R. Kumar, K. Kandpal and P. Kumar, *J. Electron. Mater.*, 2020, 1–8.

38 C.-Y. Chang, Y. K. Fang and S. M. Sze, *Solid-State Electron.*, 1971, **14**, 541–550.

39 Y. Liu, in *IOP Conference Series: Materials Science and Engineering*, IOP Publishing, 2020, vol. 738, p. 12007.

40 F. Ahmad, R. Singh, P. K. Misra, N. Kumar, R. Kumar and P. Kumar, *J. Electron. Mater.*, 2018, **47**(12), 6972–6983.

41 N. N. K. Reddy and V. R. Reddy, *Bull. Mater. Sci.*, 2012, **35**, 53–61.

42 A. Turut, H. Doğan and N. Yıldırım, *Mater. Res. Express*, 2015, **2**, 96304.

43 P. Ghaemi, R. S. K. Mong and J. E. Moore, *Phys. Rev. Lett.*, 2010, **105**(16), 166603.

44 B. Poudel, Y. Ma, Y. Lan, B. Yu, X. Yan, D. Wang, Z. Ren, Q. Hao, A. Minnich, A. Muto, D. Vashaee, X. Chen, G. Chen, J. Liu and M. S. Dresselhaus, *Science*, 2008, **320**(5876), 634–638.

45 M. Busl, G. Platero and A.-P. Jauho, *Phys. Rev. B: Condens. Matter Mater. Phys.*, 2012, **85**, 155449.

46 H. Zhang, J. Yao, J. Shao, H. Li, S. Li, D. Bao, C. Wang and G. Yang, *Sci. Rep.*, 2014, **4**, 1–5.

47 O. V. Kibis, *Phys. Rev. B: Condens. Matter Mater. Phys.*, 2010, **81**, 165433.

48 Y. Zhou and M.-W. Wu, *Phys. Rev. B: Condens. Matter Mater. Phys.*, 2011, **83**, 245436.

49 Y. H. Wang, H. Steinberg, P. Jarillo-Herrero and N. Gedik, *Science*, 2013, **342**, 453–457.

50 S. M. Sze, *Semiconductor devices: physics and technology*, John Wiley & Sons, 2008.

51 J. Dheepa, R. Sathyamoorthy, A. Subbarayan, S. Velumani, P. J. Sebastian and R. Perez, *Sol. Energy Mater. Sol. Cells*, 2005, **88**, 187–198.

52 I. Hussain, M. Y. Soomro, N. Bano, O. Nur and M. Willander, *J. Appl. Phys.*, 2012, **112**, 64506.

53 Y. Shi, Q. Zhou, A. Zhang, L. Zhu, Y. Shi, W. Chen, Z. Li and B. Zhang, *Nanoscale Res. Lett.*, 2017, **12**, 1–6.

54 F. Ahmad, R. Kumar, S. S. Kushvaha, M. Kumar and P. Kumar, *npj 2D Mater. Appl.*, 2022, **6**, 12.

55 B. M. Fregoso, Y. H. Wang, N. Gedik and V. Galitski, *Phys. Rev. B: Condens. Matter Mater. Phys.*, 2013, **88**, 155129.

56 D. Hsieh, Y. Xia, L. Wray, D. Qian, A. Pal, F. Meier, J. Osterwalder, G. Bihlmayer, C. L. Kane and Y. S. Hor, *Science*, 2009, **323**, 919–922.

57 Z.-H. Pan, A. V. Fedorov, D. Gardner, Y. S. Lee, S. Chu and T. Valla, *Phys. Rev. Lett.*, 2012, **108**, 187001.

58 H. J. Stocker, *Phys. Rev. Lett.*, 1967, **18**, 1197.

59 J.-X. Qin, X.-G. Yang, C.-F. Lv, Y.-Z. Li, X. X. Chen, Z.-F. Zhang, J.-H. Zang, X. Yang, K.-K. Liu and L. Dong, *J. Phys. Chem. Lett.*, 2021, **12**, 4079–4084.

60 N. K. Tailor, C. A. Aranda, M. Saliba and S. Satapathi, *ACS Mater. Lett.*, 2022, **4**, 2298–2320.

61 Y. Dong, K. M. Dowling, S. P. Hau-Riege, A. Conway, L. F. Voss and S. Rakheja, *J. Appl. Phys*, 2022, **113**, 134504.

62 X. Lin, X. Huang, Q. Zhang, J. Yi, S. Liu and Q. Liang, *Appl. Phys. Lett*, 2023, **123**(18), 180501.

63 E. Faella, K. Intonti, L. Viscardi, F. Giubileo, A. Kumar, H. T. Lam, K. Anastasiou, M. F. Craciun, S. Russo and A. Di Bartolomeo, *Nanomaterials*, 2022, **12**, 1886.

64 Z. Zhang, S. Wang, C. Liu, R. Xie, W. Hu and P. Zhou, *Nat. Nanotechnol.*, 2022, **17**, 27–32.